Benchmarking three low-cost, low-maintenance cloud height measurement systems and ECMWF cloud heights against a ceilometer

P. Kuhn[1,*]

Plataforma de Almería, Ctra. de Senés s/n km 4, 04200 Tabernas, Spain

M. Wirtz[1], N. Killius[2], S. Wilbert[1], J. L. Bosch[3], N. Hanrieder[1], B. Nouri[1], J. Kleissl[4], L. Ramirez[5], M. Schroedter-Homscheidt[2], D. Heinemann[6], A. Kazantzidis[7], P. Blanc[8], R. Pitz-Paal[9]

Abstract

Cloud height information is crucial for various applications. This includes solar nowcasting systems. Multiple methods to obtain the altitudes of clouds are available. In this paper, cloud base heights derived from the European Centre for Medium-Range Weather Forecasts (ECMWF) and three low-cost and low-maintenance ground based systems are presented and compared against ceilometer measurements on 59 days with variable cloud conditions in southern Spain. All three ground based systems derive cloud speeds in absolute units

*Corresponding author
Email address: pascal.kuhn@dlr.de (P. Kuhn)
[1]German Aerospace Center (DLR), Institute of Solar Research, Plataforma Solar de Almería, Ctra. de Senés s/n km 4, 04200 Tabernas, Spain.
[2]German Aerospace Center (DLR), Earth Observation Center, 82234 Weßling - Oberpfaffenhofen, Germany.
[3]Departamento de Ingeniería Eléctrica y Térmica, Universidad de Huelva, Campus de La Rábida, Carretera de Palos de la Frontera S/N 21071 La Rábida, Palos de la Frontera (Huelva)
[4]Dept. of Mechanical and Aerospace Engineering, UCSD Center for Energy Research, University of California, 92093-0411 La Jolla, USA.
[5]CIEMAT, Energy Department - Renewable Energy Division. Av. Complutense, 40, 28040 Madrid, Spain.
[6]Energy Meteorology Unit, Energy and Semiconductor Research Laboratory, Institute of Physics - Oldenburg University, 26111 Oldenburg, Germany.
[7]Laboratory of Atmospheric Physics, Department of Physics, University of Patras, 26500 Patras, Greece.
[8]MINES ParisTech, PSL Research University, Centre Observation, Impacts, Energy (O. I. E.), CS 10207, F-06904, Sophia Antipolis CEDEX, France.
[9]German Aerospace Center (DLR), Institute of Solar Research, Linder Höhe, 51147 Cologne, Germany.

of [m/s] from which cloud heights are determined using angular cloud speeds derived from an all-sky imager. The cloud speed in [m/s] is obtained from (1) a cloud shadow speed sensor (CSS), (2) a shadow camera (SC) or (3) derived from two all-sky imagers.

Compared to 10-minute median ceilometer measurements for cloud heights below 5000 m, the CSS-based system shows root-mean squared deviations (RMSD) of 996 m (45 %), mean absolute deviations (MAD) of 626 m (29 %) and a bias of -142 m (-6 %). The SC-based system has an RMSD of 1193 m (54 %), a MAD of 593 m (27 %) and a bias of 238 m (11 %). The two all-sky imagers based system show deviations of RMSD 826 m (38 %), MAD of 432 m (20 %) and a bias of 202 m (9 %). The ECMWF derived cloud heights deviate from the ceilometer measurements with an RMSD 1206 m (55 %), MAD of 814 m (37 %) and a bias of -533 m (-24 %).

Due to the multi-layer nature of clouds and systematic differences between the considered approaches, benchmarking cloud heights is an extremely difficult task. The limitations of such comparisons are discussed.

This study aims at determining the best approach to derive cloud heights for camera based solar nowcasting systems. The approach based on two all-sky imagers is found to be the most promising, having the overall best accuracy and the most obtained measurements.

Keywords: Cloud height determination, All-sky Imager, Cloud shadow speed sensor, Shadow camera

---

Contents

1. Introduction

Due to the success of solar power and the variability of the solar resource, several countries have introduced regulations regarding maximum negative ramp rates for photovoltaic (PV) plants on one-minute timescales (e.g. Puerto Rico: 10 % of nameplate capacity per minute (Lave et al., 2013), (Marcos et al., 2014)). These regulations can be fulfilled with (1) batteries, (2) by voluntarily reducing the electric output and thus being able to buffer from this reserve, (3) by using nowcasting systems or by applying a combination of these methods (Chen et al. (2017), Kuhn et al. (2017a)).

For the next minutes ahead, the solar variability originates from transient clouds. Clouds shading a solar power plant can significantly and rapidly reduce the amount of dispatched electricity. Such steep ramps threaten the stability of the electricity grid and need to be avoided (Perez et al., 2016).

Satellites have many applications for solar forecasting (Hammer et al. (1999), Cros et al. (2014)). However, they do not have sufficient temporal and spatial resolution to predict ramp rates on one-minute timescales. Nowcasting systems for this purpose can be based on cameras (all-sky imagers) on the ground near the plant (Urquhart et al. (2013), Nguyen et al. (2016), Kazantzidis et al. (2017)) or sensor grids (Chen et al., 2017).

All-sky imager based nowcasting systems consist of at least one camera taking photos of the sky. In these photos, clouds are segmented (e.g. Kazantzidis et al. (2012), Yang et al. (2014)), their shadows are projected on the ground and spatially resolved irradiance maps are calculated (Kuhn et al., 2017a). With cloud velocities derived, predictions can be made which help to optimize operations in industrial solar power plants (Fernandez-Jimenez et al., 2012).

For such camera based nowcasting systems, cloud height information is crucial: If the altitude of a cloud at 45° sun elevation is determined 3 km away from the actual cloud height, the shadow of this cloud is assumed to be 3 km away from its real position (see Fig. 1). Here, we compare the performance of five methods for estimating cloud heights for solar nowcasting applications. These systems are (1) a ceilometer, acting as the reference, (2) cloud height data from the numerical weather prediction model (NWP) of the European Centre for Medium-Range Weather Forecasts (ECMWF), (3) an adapted system based on a cloud shadow speed sensor (CSS) and one all-sky imager (ASI-CSS), (4) a novel system consisting of one all-sky imager and a shadow camera (ASI-SC) and (5) a novel approach based on two all-sky imagers (ASI-ASI). Cloud heights can be determined by ceiling balloons and radiosondes as in-situ observations (Wang and Rossow, 1995), which is however not feasible for nowcasting systems: The temporal resolution is too small and their application too labor and cost intensive.

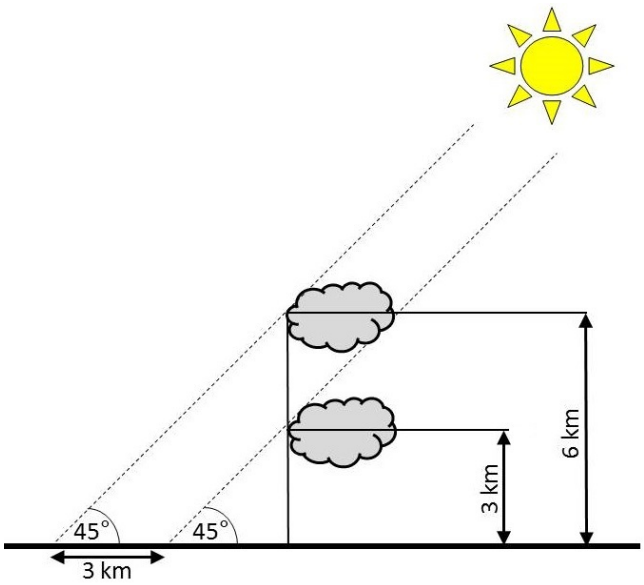

Figure 1: Example situation highlighting the relevance of cloud heights for solar nowcasting applications: The correct temporal predictions of shading events strongly depend on cloud heights. Deviations in the determined cloud heights lead to deviations of the predicted shading time.

All systems are studied in the complex cloud conditions present at the Plataforma Solar de Almería (PSA), Spain, on 59 days. This way, the five approaches (ceilometer, ASI-CSS, ASI-SC, ASI-ASI, NWP) can be directly benchmarked: As the deviations strongly depend on the weather conditions and the benchmarking periods, comparing different systems must be done using the same period and location.

This paper is structured as follows: After the introduction, we will discuss the difficulties of comparing various cloud height measurement systems in section 2. The hardware and methodology are explained in section 3. All systems are benchmarked in section 4. The conclusion is given in section 5.

2. On the difficulties of cloud height analyses

To benchmark the obtained cloud heights, a ceilometer (CHM 15k NIMBUS, G. Lufft Mess- und Regeltechnik GmbH) is used, located approximately 7 m and 8.5 m away from the main all-sky imager and the CSS, respectively (see Fig. 2). The ceilometer is also within the area imaged by the shadow camera. The ceilometer can output several cloud heights. Only the main cloud height is used here. Cloud heights are derived from post-processing the ceilometer raw data. In Martucci et al. (2010), comparing this model to another ceilometer (CL31, Vaisala), an average bias of 160 m and a coefficient of determination $R^2 = 0.788$ are found.

In addition to systematic deviations of the reference measurements, the cloud base heights (CBH) measured by the ceilometer are not physically identical to cloud heights derived by the other considered systems:

The NWP cloud heights from the ECMWF model are derived for a large area of $0.125^\circ \times 0.125^\circ$ (latitude/longitude), which corresponds to 13.5 km $\times$ 11 km at the site. The local topography is thus only partially considered. Besides the spatial resolution, the temporal resolution is limited as well. Furthermore, only one cloud height is calculated and the modeling of cirrus clouds is difficult. Comparisons of such spatially and temporally aggregated NWP cloud heights

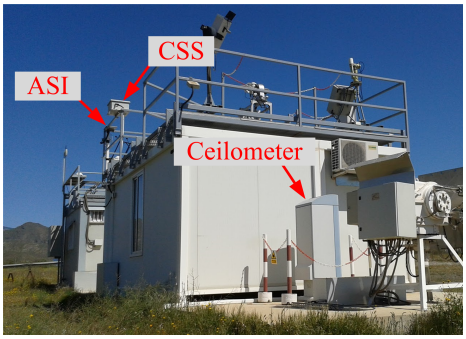

Figure 2: All hardware used for the ASI-CSS system and its benchmarking is located in close proximity: Ceilometer on the right, all-sky imager on the top-left (above the antenna) and the CSS approximately 1.5 m right of the camera.

to the point-like measurements of the ceilometer must be interpreted with care.

The CSS based cloud height measuring system (ASI-CSS) consists of an adapted cloud shadow speed sensor (Kuhn et al., 2017c) and one all-sky imager. This system utilizes an approach similar to (Wang et al., 2016). In Wang et al. (2016) cloud shadow speeds measured by the CSS and angular velocities obtained from one all-sky imager are used to derive cloud heights. This system thus combines measurements from the CSS (area: approximately 0.09 m^2) with all-sky images of 180° viewing angle. Although the CSS, the all-sky imager and the ceilometer are in close proximity, their measurements do not need to correspond to the same clouds. The ceilometer measures point-like cloud heights directly above its position whereas the CSS measures velocities of clouds shading its sensors (more explanation are given in section 3.3.2). The all-sky imager on the other hand derives angular velocities from its whole 180° viewing angle. Therefore, comparing ASI-CSS cloud heights to ceilomter measurements is also difficult.

The novel ASI-SC cloud height measurement system uses the same all-sky imager as the ASI-CSS system and a so-called shadow camera, taking images of the ground. From these images, cloud motion vectors are derived which, in combination with angular velocities measured by the all-sky imager, determine cloud heights. The shadow camera considers an area of 0.28 km^2, from which

cloud shadow speeds are derived. The clouds shading this area are usually not the clouds directly above the ceilometer, although the ceilometer is located in this area. Again, comparisons must be handled carefully.

The ASI-ASI system consists of two all-sky imagers. Using a novel differential approach, detecting clouds is not needed to derive cloud heights. The two cameras can derive heights for all clouds imaged by both cameras. Depending on the cloud heights, this is an area of several km^2. Although a special approach is used to better spatially match the thus derived cloud heights to ceilometer measurements, systematic offsets are addressed.

In general, the ASI-CSS system, as well as ASI-SC and ASI-ASI system, do not measure cloud base heights, but rather the mean height of the clouds. Mean cloud heights are measured as the all-sky imager usually derives angular cloud velocities, which correspond rather to the mean angular velocity of the whole cloud than to the angular velocity of the lower end of the clouds. The same argument holds for the measurements of the shadow speeds. Therefore, the cloud heights derived by the presented systems are rather linked to an average cloud height than to the cloud base heights measured by the ceilometer. In section 4.1, we discuss these systematic offsets for two example days.

3. Cloud height measurements systems

3.1. Ceilometer as a reference

We know that ceilometer results "*show significant offsets between the two manufacturer-derived cloud base heights along with a considerable degree of scatter*" (Martucci et al. (2010), Vaisala CL31 and Jenoptik CHM15K show an average instrument CBH offset of 160 m) and measure different cloud heights in comparison to the benchmarked systems (see discussion previous section 2). Nonetheless, we consider the ceilometer (CHM 15k NIMBUS, G. Lufft Mess- und Regeltechnik GmbH) to be acceptable for careful comparisons.

3.2. NWP cloud height data from the ECMWF model

Cloud heights obtained from a numerical weather prediction (NWP) model are compared to ceilometer measurements. The NWP model used for our study is the Integrated Forecast System (IFS) operated by the European Centre for Medium-Range Weather Forecasts (ECMWF), which provides cloud base heights. The NWP data are available at an hourly resolution for historic data and have a 3 h temporal resolution for operationally usable, predicted (future) timestamps for the day-ahead electricity market participation without extra costs.

3.3. Three ground based cloud height measurement systems

3.3.1. Deriving angular velocities from one all-sky imager

Using an all-sky imager, a cloud height can be derived if the cloud velocity in [m/s] and an angular velocity are known (Wang et al., 2016). The angular cloud velocity in [pixel/s] is derived from clouds detected in orthogonal images, which were undistorted from the raw images in fisheye projection. Segmenting all-sky images is a surprisingly difficult task, which is avoided here by using a novel differential approach.

In Fig. 3, the novel approach to derive cloud motion vectors in [pixel/s] without cloud detection within the images is visualized. A total of three subsequent images are utilized (in this example 2015-09-19; 10:25:00 h, 10:25:30 h, 10:26:00 h; UTC+1). Only one color channel of the RGB images is used. Results derived from the different color channels deviate insignificantly. In the following, the blue color channel is used. We use a color channel and not the red-to-blue ratio to exploit a specific effect:

If the calculations are conducted using the red-to-blue ratio, clouds all over the sky would contribute equally to the general derived cloud height. On the other side, if a color channel is used, cloud movements at the center and near the sun are more likely to be detected. These movements are more often detected as the absolute changes in one color channel are higher near the sun and in the center of the image than on the edges of an all-sky image. The absolute

changes in the color channels are generally smaller at the edges of an all-sky image due to vignetting. As the ceilometer is close to the all-sky imager, using only one color channel improves the spatial matching between the systems for this comparison. For nowcasting applications, the use of the red-to-blue ratio is recommended. Furthermore, individual cloud heights should be calculated. Such an approach will be presented in a future publication.

The blue channel of the current fisheye raw image is displayed in the top left corner (10:26:00 h, t_1). The previous raw image (10:25:30 h, $t_1 - \Delta t$) is displayed twice: It is the first image in the second row and the second image in the first row. The second last raw image (10:25:00 h, $t_1 - 2 \cdot \Delta t$) is shown as the second image in the second row. In a first step, difference images $d_i(x, y)$ are calculated from the image series $B(x, y, t_i)$ using Eqs. 1 and 2.

$$d_1(x, y) = B(x, y, t) - B(x, y, t - \Delta t) \tag{1}$$

$$d_2(x, y) = B(x, y, t - \Delta t) - B(x, y, t - 2\Delta t) \tag{2}$$

x and y are the pixel coordinates in the images, t is the timestamp. For the all-sky imager, the temporal resolution is $\Delta t = 30$ s. The absolute values of the difference images are undistorted from the fisheye projection into an horizontal projection (arrows, $o_i(m, n)$). A dynamic threshold is calculated as the 98th percentile of all pixel values in the considered all-sky image (one color channel). By applying this dynamic threshold on the absolute pixel values of $o_i(m, n)$, a dynamic threshold is found and the differential images are converted into binary images $b_i(m, n)$ (bottom row, right). The binary images are matched using a normalized 2-D cross-correlation (Huang et al., 2012). The cross-correlation is calculated using Eq. 3 with $\overline{b_i}$ being the mean of binary image i. The values which maximize u, v are determined and taken as the cloud displacement vector (Huang et al., 2012).

$$(u_{max}, v_{max}) = \frac{\sum_{m,n} \left(b_1(m, n) - \overline{b_1}\right) \left(b_2(m - u, n - v) - \overline{b_2}\right)}{\left(\left[\sum_{m,n} \left(b_1(m, n) - \overline{b_1}\right)^2 \right] \cdot \left[\sum_{m,n} \left(b_2(m - u, n - v) - \overline{b_2}\right)^2 \right] \right)^{0.5}} \tag{3}$$

By dividing the cloud displacement vector by the time between the images, the angular cloud motion vector as seen by the all-sky imager in the unit of [pixel/s] is derived. Comparable differential approaches for motion detection of persons and objects are presented in (Shuigen et al., 2009) and (Singla, 2014).

Differentiating dirt on the camera from (optically thin) clouds in singular all-sky images is often impossible even for experienced human observers. Many cloud detection approaches wrongly classify such dirt spots as clouds. With the novel differential approach, static dirt spots are not considered. Therefore, deriving cloud heights without the need to detect actual clouds is considered to be a major improvement.

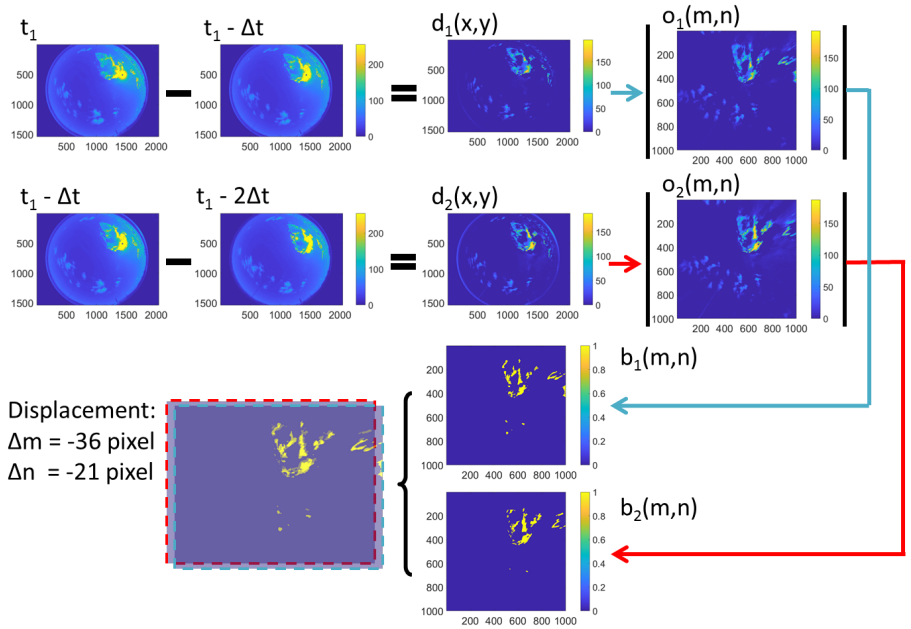

Figure 3: Cloud segmentation independent approach to derive cloud motion vectors in [pixel/s] from one all-sky imager and a total of three subsequent images: From one color channel (here: blue) of the raw images, difference images $d_i(x, y)$ are calculated. These difference images are then undistorted from the fisheye projection into the orthonormal projection ($o_i(m, n)$). Applying a dynamic threshold (here: 58 for $o_1(m, n)$ and 65 for $o_2(m, n)$) on the absolute values of the undistorted difference images allows a segmentation into binary images $b_i(m, n)$. These binary images are matched via cross-correlation. This way, a cloud motion vector in [pixel/s] is derived.

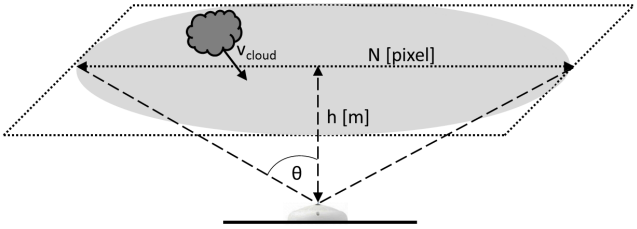

Figure 4: Visualization of the cloud height formula (equ. 4). v_{cloud} is derived both in [m/s] and in [pixel/s]. The circle defined by θ has a diameter of N pixels. The cloud layer is at height h.

If a cloud's angular velocity $v_{pixel/s}$ is derived and its velocity $v_{m/s}$ is known, the cloud height h can be determined via Eq. 4 (Wang et al., 2016).

$$h = \frac{v_{m/s} N}{2 v_{pixel/s} \tan\theta} \tag{4}$$

In Eq. 4, θ is the maximum zenith angle within which the all-sky image information is used. N corresponds to the diameter of the circle defined by θ in [pixel]. For all calculations conducted in this paper, $\theta = 70°$ and $N = 1000$ pixel. This approach is further described in Wang et al. (2016) and visualized in Fig. 4.

Using Eq. 4, cloud heights can be derived from an all-sky imager (providing the angular velocity $v_{pixel/s}$) and cloud velocities $v_{m/s}$ (in [m/s]). The latter can be measured by the CSS (see section 3.3.2)), or measured by a shadow camera (see section 3.3.3) or derived from a total of two all-sky imagers (see section 3.3.4).

3.3.2. All-sky imager and cloud shadow speed sensor system (ASI-CSS)

The cloud shadow speed sensor (CSS) (see Fig. 5) is the one developed and presented in Fung et al. (2013) and was installed for this study at PSA. The CSS consists of nine simple solid state pyranometers, which are sampled at a frequency of 667 s^{-1}. Eight of the sensors are placed in a circular arc of 105° with a radius of 29.7 cm around the ninth sensor. If the shadow of a cloud moves over the CSS, the sensors detect ramps at slightly different times. This way, both the velocity and the direction of the clouds can be determined. Due to the

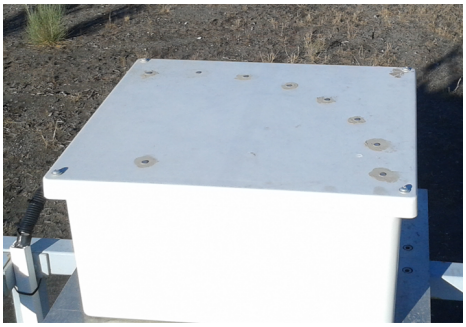

Figure 5: CSS at PSA. The 9 dots, 8 arranged in a circular arc around one in its center, are the sensors used to determine cloud shadow speeds and directions.

high measurement frequency, the distances of the sensors can be small, which enables a very compact design. The CSS does not need regular cleaning as the working principle is based on relative deviations of the irradiances measured by the nine pyranometers and not absolute irradiance measurements. During more than one year of service in a harsh desert environment, the CSS was found to be very reliable.

An in-depth field comparison (Kuhn et al., 2017c) conducted at the Plataforma Solar de Almería (PSA) on the CSS revealed that the CSS performs best for optically thick clouds. On 223 days, the CSS could only measure 4.8 % of all clouds having a transmittance above 70 % and a shading duration above 10 minutes (Kuhn et al., 2017c). Even fewer measurements were obtained for clouds with shading durations between 1 and 10 minutes and transmittances above 70 %. The CSS is best for clouds with shading durations below 1 minute and transmittances below 40 %, for which 21.6 % of all shadows are measured (Kuhn et al., 2017c). Adaption of the CSS algorithm resulted in an increase of 91 % more cloud motion measurements for the 59 days considered here (Kuhn et al., 2017c). However, this adaption results in reduced accuracy. The adaption is considered necessary as the detection rate of the CSS is very low. For solar nowcasting application, a less accurate measurement might be preferable to no measurement at all. All benchmarks were also conducted for the unmodified CSS, still showing higher deviations in comparison to the ASI-ASI or ASI-SC

Figure 6: The off-the-shelf surveillance camera (Mobotix Q24M Hemispheric) used in combination with the CSS (and the systems presented in section 3.3.3 and 3.3.4) to determine cloud heights.

system (not shown).

The all-sky imager used (see Fig. 6) to determine clouds heights is an off-the-shelf surveillance camera (Mobotix Q24M Hemispheric). The camera takes an hemispherical image every 30 seconds with a resolution of 2048 × 1536 pixels (Wilbert et al., 2016). The camera is located approximately 1.5 m away from the CSS and approximately 7 m away from the ceilometer. Thus, the used hardware of the ASI-CSS system is located in close proximity (see Fig. 2). The total cost of this system's hardware is the price of one all-sky imager (approximately 800 €) and the CSS, whose material costs are specified to be less than 400 USD (Wang et al., 2016).

3.3.3. All-sky imager and shadow camera system (ASI-SC)

As demonstrated in section 3.3.1, cloud heights can be derived from an all-sky imager and the cloud velocities in [m/s]. In this section, a novel camera based approach is presented, which also derives absolute cloud speeds in [m/s]: A shadow camera takes photos of the ground from an 87 m high tower (CIEMAT CESA-I, see Fig. 7). The camera is also part of the shadow camera system described in (Kuhn et al., 2017b), which provides spatially resolved irradiance maps. In 2018, the shadow camera system was elected among the top 5 of *emerging technologies in solar forecasting* (Yang et al., 2018). Further potential applications of shadow cameras are presented in (Kuhn et al., 2018).

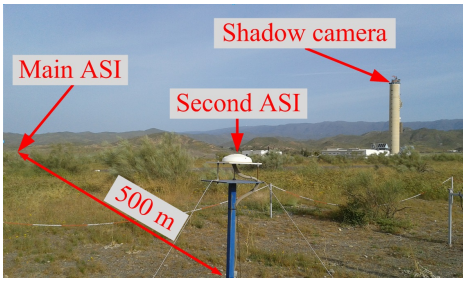

Figure 7: Position of the second all-sky imager (ASI) approximately 500 m away from to the main all-sky imager and approximately 540 m away from the shadow camera (CIEMAT CESA-I tower on the right).

Every 15 s, the camera (Mobotix MX-M24M-Sec-D22, CMOS sensor) takes an 8 bit RGB image of 2048 × 1536 pixels. An example raw image is displayed in Fig. 8 (left). Both an interior, an external orientation and a ground model is needed to obtain the distorted orthoimage in Fig. 8 (right). The ground model is calculated from a grid of GPS reference points. The interior orientation is determined using methods presented in Scaramuzza et al. (2006). The external orientation is derived using GPS reference coordinates of objects visible in the images.

In order to derive cloud velocities under realistic conditions, a quadratic area of 105 × 105 pixels within the orthoimage is used, which corresponds to a 525 m × 525 m large area.

The approach to derive cloud shadow speeds from a shadow camera is very similar to the approach developed for the all-sky imagers in order to detect cloud speeds in [pixel/s] (see section 3.3.1):

From three subsequent images corresponding to timestamp t, t-Δt and t-$2\Delta t$, the cloud shadow speed is derived. By subtracting the three gray images, two difference images d_i are calculated from the three orthoimages. The first difference image d_1 for timestamp t is the absolute of the subtraction of orthoimage t and orthoimage t-Δt. The second difference image d_2 is the absolute of the subtraction of the orthoimages t-Δt and t-$2\Delta t$. For the shadow camera, the image acquisition rate is $\Delta t = 15$ s.

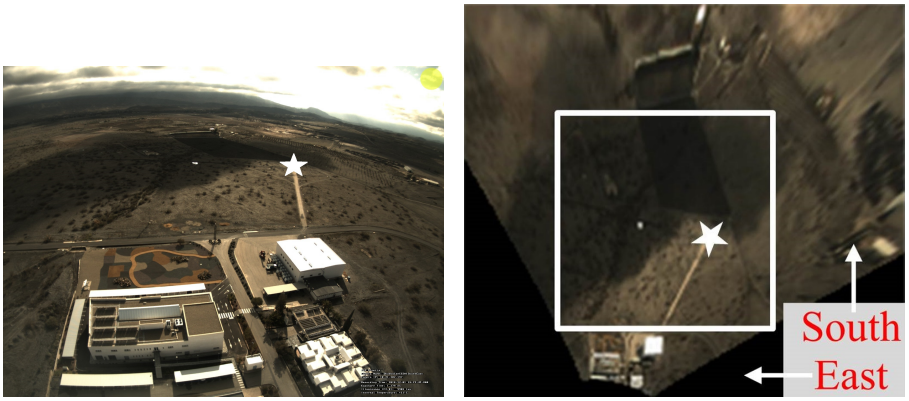

Figure 8: Left: Raw image of the used shadow camera. Right: Undistorted raw image as projected on a ground model, corresponding to Fig. 8a. The white frame marks the 525 m × 525 m large area in which cloud shadow speeds are determined. The white stars in both images mark the positions of the ceilometer, the CSS and the all-sky imager used both in the ASI-CSS and the ASI-SC system (see Fig. 2 for a close-up).

The absolute values of the difference images are converted into binary images by a dynamic threshold, based on the 98th percentile of each difference image. In order to determine the cloud shadow speeds, the pixel displacement Δx and Δy between the two difference images is obtained by the normalized 2-D cross-correlation approach presented in Huang et al. (2012).

From the displacement vector, the cloud shadow speed can be derived using Eq. 5.

$$v = \frac{\sqrt{(\Delta x)^2 + (\Delta y)^2}}{\Delta t} \times k_{SC} \tag{5}$$

Δt is the temporal resolution, N is length of the quadratic imaged area in pixel and k_{SC} is the ratio of meters per pixel in the orthoimages. From a technical point of view, the cameras can take several images each second. However, the produced data sets would be huge. Due to the temporal resolution of $\Delta t = 15$ s, the shadow camera can currently only reliably resolve cloud shadow speeds up to 17.5 m/s (Kuhn et al., 2017c). This limit is derived by looking at a cloud crossing the area under consideration in parallel to its borders. This is the extreme case. For other cloud movement directions greater velocities up to

49.5 m/s can be resolved (not considered in the comparisons). Although the majority of clouds in this area have velocities below 17.5 m/s (Kuhn et al., 2017c), this is a disadvantage. If a shadow camera is only used to derive real-time cloud speeds and directions, then the raw images would not have to be stored and image acquisition frequency would not be limited by storage space considerations. The limiting factor would then be the required processing time. For the shadow camera, the processing time can be below 1 s.

The approach described is this section is only feasible if an area with little non-cloud movements and not many specularly reflecting objects as well as an elevated position is available. The total cost of this system's hardware is the price of one all-sky imager (approximately 800 €) and one shadow camera (approximately 700 €).

3.3.4. Two all-sky imager system (ASI-ASI)

Many approaches to derive cloud heights based on two (or more) all-sky imagers are published (e.g. Allmen and Kegelmeyer Jr (1996), Kassianov et al. (2005), Seiz et al. (2007), Nguyen and Kleissl (2014), Beekmans et al. (2016) and Blanc et al. (2017)). To the best of our knowledge, all all-sky imager based approaches to derive cloud heights depend on cloud detection or re-finding special points of interest within images, which might be a main origin of errors (Bernecker et al., 2013). In this section, we present a novel cloud segmentation-independent approach to determine cloud heights via two all-sky imagers. This approach may hypothetically cope better with less frequent cleaning routines of the all-sky imagers than other approaches.

In addition to the all-sky imager presented in section 3.3.2, another identical all-sky imager 496.7 m away from the first camera is used for this approach (see Fig. 7). From both all-sky imagers, one orthogonalized difference image is calculated using the approach explained in in section 3.3.1. Based on the two difference images from the two all-sky imagers, corresponding to the same timestamps, and the known distance between these cameras, the velocity in [pixel/s] (derived as explained in section 3.3.1) can be transferred to a velocity

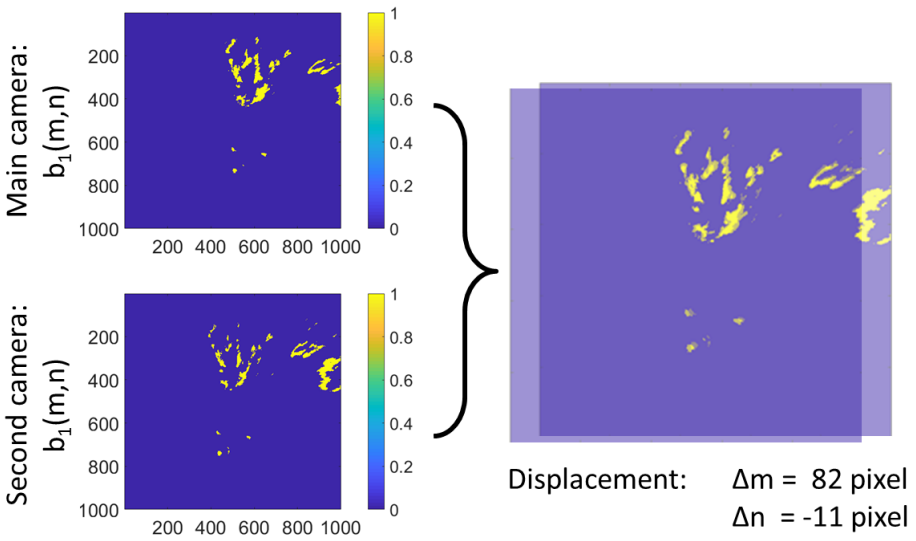

Figure 9: Deriving cloud motion vectors in [m/s] from two all-sky imagers: The binary difference images $b_i(m,n)$ of two difference all-sky imagers are matched. The found displacement in [pixel] corresponds to the distance of the cameras, which is known.

in [m/s]. Thus, cloud heights can be derived (see section 3.3.1 and Eq. 4).

Figure 9 visualizes this approach: In the top left corner, the first binary difference image $b_1(m,n)$ of Fig. 3 is displayed. In the bottom left corner, the corresponding binary difference image of the second all-sky imager is presented. The displacement between these images is calculated by matching the images via the normalized 2-D cross-correlation (Eq. 3, two images on the right, Fig. 3). This provides a vector $[\Delta m, \Delta n]$. From this vector, the absolute displacement d_{pixel} in pixels can be calculated by $d_{pixel} = \sqrt{\Delta m^2 + \Delta n^2}$. As the distance between the cameras is known (496.7 m) and the displacement d_{pixel} results from the different positions of the all-sky imagers, one pixel in the orthoimages can be assigned to have a certain distance in [m]. From this relation, the derived cloud speeds in [pixel/s] are transformed to a velocity in [m/s]. With this velocity and the approach explained in section 3.3.1, cloud heights can be determined.

The total cost of this system's hardware is the price of the two used cameras (approximately 800 € each).

4. Benchmarking of the cloud height systems against ceilometer measurements

This section is structured as follows: Two example days are studied in detail in section 4.1. In section 4.2, the ASI-CSS system is benchmarked, followed by the ASI-SC system in section 4.3. The system consisting of two cameras (ASI-ASI) is compared to ceilometer data in section 4.4. In section 4.5, deviations of the NWP cloud base heights in comparison to the ceilometer are presented. The histograms of the cloud heights as measured by the five systems are displayed in section 4.6. Statistical deviations metrics for all system in comparison to the ceilometer as derived from 59 days are presented in section 4.7. Section 4.8 compares the found deviations to the literature.

The benchmarking methodology is the same for all systems: All determined cloud speeds ($v_{pixel/s}$ and $v_{m/s}$) are filtered by a 10-minute median and the corresponding heights are compared to the 10-minute median of the ceilometer measurements. Cloud heights above 15 km are ignored. For the cloud heights predicted by the ECMWF model, the 180 minute resolution is chosen. These values are considered to be the mean values of 180 min.

4.1. Two example days

In this section, cloud heights derived from all considered systems (ceilometer, ASI-CSS, ASI-SC, ASI-ASI, NWP) are compared to each other on two example days, 2016-09-01 and 2016-05-12. This section is intended to illustrate the systematic offsets discussed in section 2.

In Fig. 10, cloud heights on 2016-09-01 are displayed. During the morning, a scattered cloud layer with a constant height of approximately 1000 m is measured by all ground-based systems. The NWP derived cloud height underestimates this altitude, which changes in the forecast valid after 13:00 h (UTC+1).

In the afternoon, clouds at higher altitudes are measured. Both the ASI-ASI system and the ASI-SC system correctly predict the general cloud height

with the ASI-ASI system being closer to the ceilometer. The ASI-CSS system significantly underestimates the cloud heights for reasons discussed later in section 4.2. The NWP derived cloud heights deviate from all other measurements. For the ASI-CSS system, 371 out of 561 total measurements could be temporally matched with 10-minute median ceilometer measurements. Thus, for 190 cloud heights obtained by the ASI-CSS system, no corresponding ceilometer measurements were made. For the ASI-SC system, 257 of 349 measurements could be temporally matched and for the ASI-ASI system 434 out of 709 measurements. In Fig. 11, a more complex day (2016-05-12) is displayed. On this

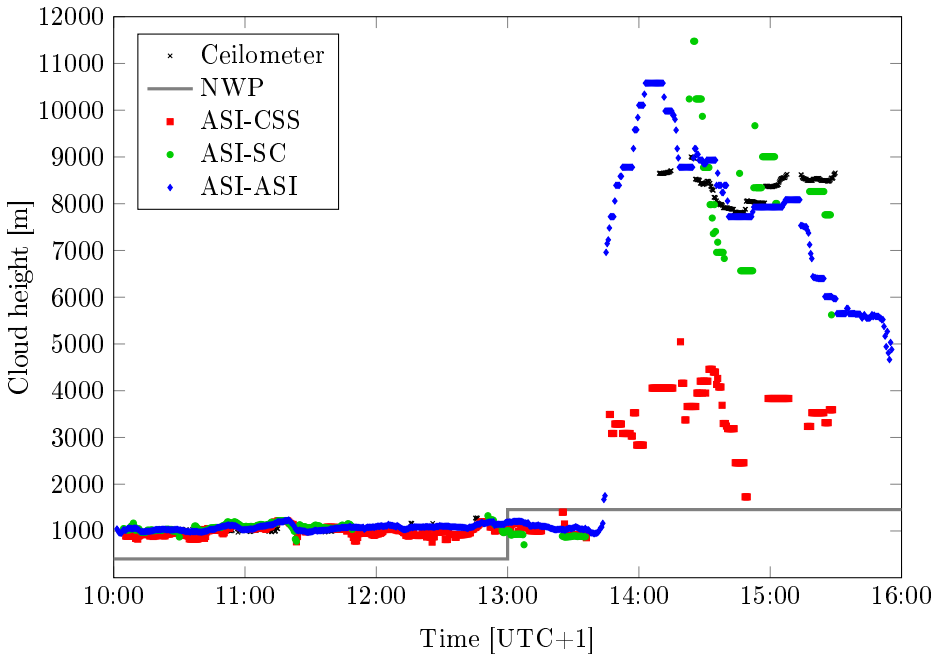

Figure 10: Cloud heights from all considered systems on 2016-09-01. Between 10:00 (UTC+1) and 14:00, all measurements show altitudes of approximately 1000 m. In the afternoon, clouds with higher altitudes are measured. Ceilometer measurements are depicted without temporal averaging, the other ground-based systems are depicted for 10-minute moving medians.

day, clouds at various altitudes are present. At noon, the ceilometer measures several clouds at approximately 6000 m, which are not measured by other systems. This effect originates from the chosen difference image based approach

using a dynamic threshold: If both optically thick and optically thin clouds are present, the ground-based systems (ASI-CSS, ASI-SC, ASI-ASI) are more likely to measure optically thick clouds (see section 3.3.1 and section 3.1). Figure 12

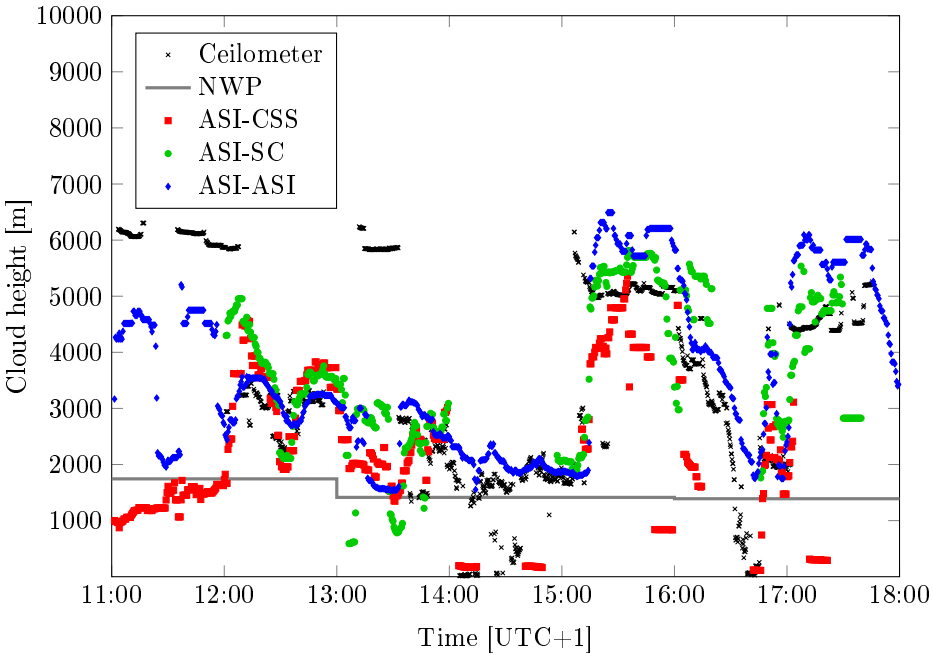

Figure 11: Derived cloud heights from all considered systems on 2016-05-12. Clouds at various heights are present on this day. Ceilometer measurements are depicted without temporal averaging, the other ground-based systems are depicted for 10-minute moving medians.

illustrates this effect with an all-sky image taken on 2016-05-12 at 13:19:30 h (UTC+1). Both cumulus (e.g. top right) and cirrus clouds (left-center) are visible. As the all-sky imager is located in close proximity to the ceilometer (see Fig. 2), the ceilometer measures at this point of time a cirrus cloud in the zenith of the image (see Fig. 11). Other systems (ASI-ASI, ASI-SC, ASI-CSS) are more likely to measure the heights of the optically thick clouds. For many solar energy specific applications, e.g. ramp-rate prediction systems, optically thick clouds are far more important. As demonstrated, in the presence of optically thick and optically thin clouds, the ceilometer may measure the height of the optically thin cloud above its position whereas the ASI-SC and ASI-ASI

system tend to measure heights of the optically thick clouds. Therefore, the cloud heights obtained by the ASI-SC and ASI-ASI system might arguably be better suited for nowcasting applications than the point-like of the ceilometer.

Earlier that day, between 11 h and 12 h, optically thin clouds are shading the CSS whereas optically thick clouds are coming from the west. These optically thick clouds dissolve completely before casting shadows on the CSS, but are seen by the all-sky imager. Thus the ASI-CSS system matches fast velocities of optically thin clouds at about 6 km (as measured by the ceilometer) with optically thick clouds at lower altitudes. This way, the ASI-CSS system provides cloud height measurements which deviate from the ceilometer measurements. During this time, the ASI-SC system does not provide measurements, which is caused by the optically thin clouds having cloud speeds above the maximum resolvable velocity. As the optically thin clouds are near the sun and the optically thick clouds are away from the sun, their induced changes in the color channels of the all-sky imager are similar. The ASI-ASI system thus tries to match the detected movements into one cloud height, which results in an average cloud height between 4 km and 5 km. At 11:30 h, some thick clouds approach from the west while no optically thin cloud is next to the sun. This leads to a presumably correct measurement of 2 km. All approaching clouds dissolve before reaching the ceilometer position.

On 2016-05-12, the ASI-ASI system derived 838 measurements of which 791 could be temporally matched to ceilometer measurements (10-minute medians). The ASI-SC system derived 511 measurements, of which 493 could be temporally matched. For the ASI-CSS system 540 from 577 total measurements could be temporally matched.

In Fig. 11, periods in which not all systems provide measurements can be seen. This is caused by clouds not being directly above the ceilometer, by clouds not directly shading the CSS or, for the ASI-SC system, by clouds having velocities above the maximum resolvable velocity of 17.5 m/s. The ASI-ASI system, which derives a cloud height if there is any movement in the sky at all, delivers a cloud height every 30 s. For the 7 h considered on this day, this

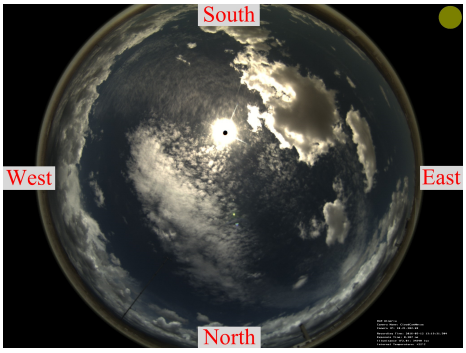

Figure 12: All-sky image taken on 2016-05-12 at 13:19:30 h (UTC+1). Both cumulus and cirrus clouds are visible. As the all-sky imager is located in close proximity to the ceilometer, the ceilometer measures at this point of time a cirrus cloud (see Fig. 11). Other systems (ASI-CSS, ASI-SC, ASI-ASI) measure the heights of the cumulus clouds.

would result in 840 measurements. Due to the differential approach needing two previous images, this is reduced to 838 measurements. The NWP derived cloud height is relatively constant on this day and generally underestimates the cloud heights.

4.2. Benchmarking of the all-sky imager and cloud shadow speed sensor system (ASI-CSS)

Figure 13 visualizes the cloud height deviations found between the ASI-CSS system, based on one all-sky imager and the cloud shadow speed sensor, and the reference ceilometer as presented in Table 2. In this scatter density plot, cloud heights derived from both the ASI-CSS system and the ceilometer are compared with a bin size of 200 m. The color shows the relative frequency of the temporally matched cloud heights within each ceilometer cloud height bin. This means that the relative frequencies in one column, which is one ceilometer cloud height bin, adds up to 100 %. The results are displayed again for 10 minute medians derived from the ASI-CSS system and compared to 10-minute median measurements of the ceilometers. For low cloud altitudes, the measurements align well (compare with Table 2). However, the ASI-CSS system is not able to measure clouds at high altitudes correctly. A detailed field study (Kuhn

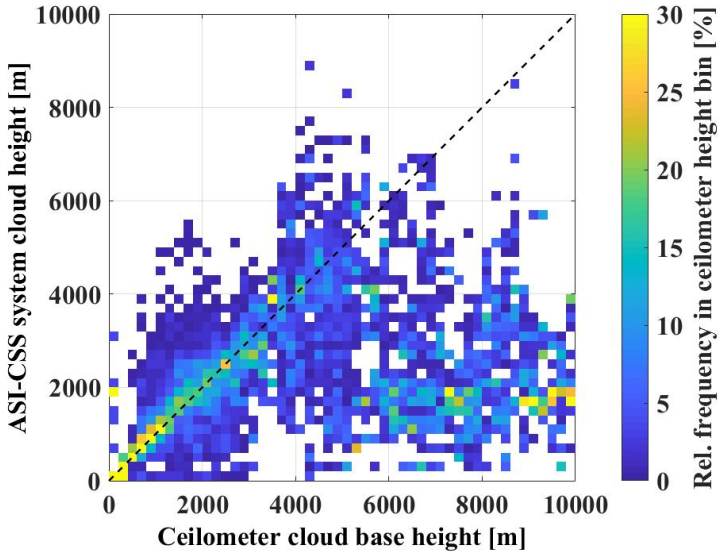

Figure 13: Scatter density plot for cloud heights on 59 days obtained with CSS.

et al., 2017c) revealed that this is caused by optically thin clouds, which are not measured with high accuracy by the CSS. In many cases, optically thin clouds are at a high altitude, which leads to a significant negative bias of -1546 m. For clouds below 5000 m, the bias is reduced to -174 m (see Table 2). In Wang et al. (2016), this behavior of the CSS is anticipated, but could not be studied in detail due to generally low cloud heights in San Diego.

As discussed in section 2 and demonstrated in section 4.1, there are systematic offsets: The cloud base height measured by the ceilometer and the cloud heights derived by the ASI-CSS system are not identical: The ceilometer measures only clouds directly above its position and the CSS measures only clouds which directly shade it. Although the all-sky-imager, the CSS and the ceilometer are located in close proximity (see Fig. 2), the clouds measured by the ASI-CSS system and by the ceilometer are not the same (see discussion in section 4.1). This is partially compensated by the 10-minute filtering, but systematic deviations still remain.

4.3. Benchmarking of the all-sky imager and shadow camera system (ASI-SC)

The deviations of the ASI-SC system are visualized in Fig. 14 in the same way as in section 4.2 for the ASI-CSS system. In comparison to the ASI-CSS system (see section 4.2), the ASI-SC system is able to determine optically thin clouds at high altitudes. This is caused by the dynamic threshold applied to the image analysis (see section 3.3.3 for explanations). Although significant scatter is present, especially low cloud heights are determined with high accuracy. As

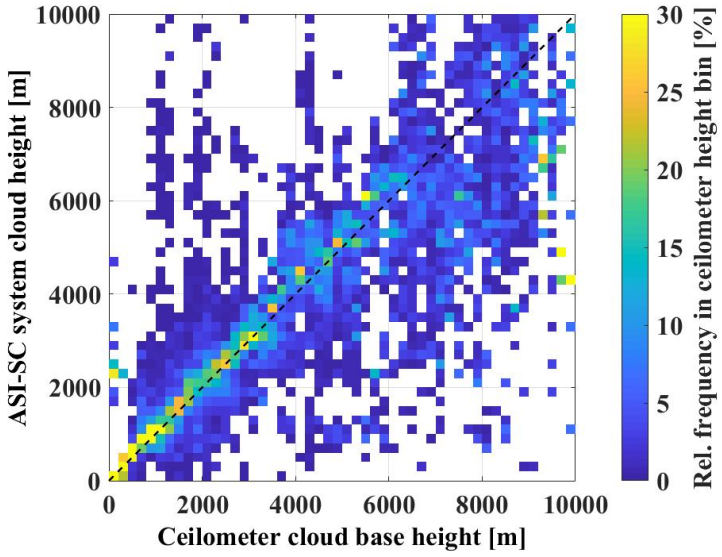

Figure 14: Scatter density plot for cloud heights on 59 days obtained with ASI-SC-system.

for the ASI-CSS system, the cloud base heights measured by the ceilometer and the cloud heights derived by the ASI-SC system are not identical: The ASI-SC system matches the velocities of the all-sky imager (see section 3.3.3) with the velocities obtained from the shadow camera. The cloud shading the ceilometer, which is seen by the shadow camera, may not be inside the field of view of the ceilometer. Therefore, a systematic deviation between the systems is present. Moreover, due to the dynamic threshold described in section 3.3.1, the ASI-SC system tends to measure the cloud heights of optically thick clouds in the

presence of multiple cloud layers. The ceilometer, however, measures the CBH directly above its position, which causes a systematic offset.

4.4. Benchmarking of the two all-sky imager system (ASI-ASI)

In section 4.7 (see Table 2), the ASI-ASI system, based on two all-sky imagers, is found to generally show lesser deviations in comparison to NWP cloud height data and the ASI-CSS system and similar deviations as the ASI-SC system. This behavior is reflected in Fig. 15. The ASI-ASI system correctly detects clouds at high altitudes. Deviations are present for clouds, which are measured by the ceilometer to have a high altitude but determined to have a low altitude by the ASI-ASI system.

We assume that a great part of these deviations are caused by the two systems measuring different clouds: Due to the dynamic threshold explained in section 3.3.4, the ASI-ASI systems predominantly determines the cloud heights of the optically thickest clouds close to the sun. If for the timestamp under consideration the ceilometer measures an optically thin cloud at a higher altitude, a systematic deviation between the systems would occur. An example for such an event is presented and discussed in section 4.1.

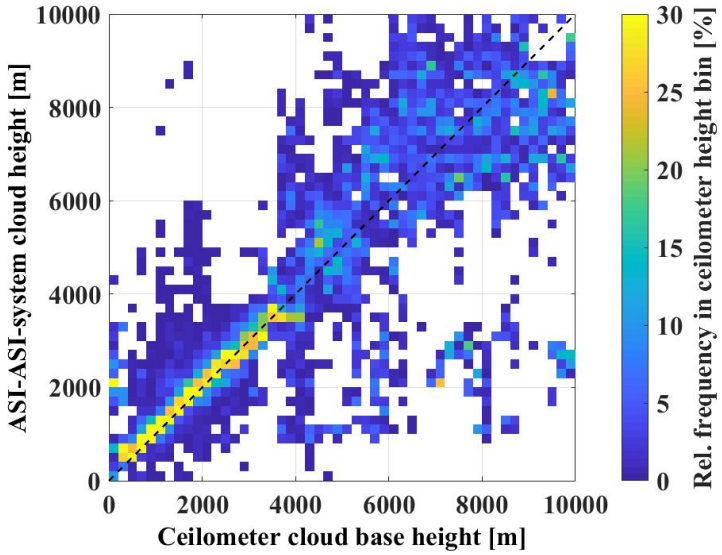

Figure 15: Scatter density plot for cloud heights on 59 days obtained with ASI-ASI-system.

4.5. Benchmarking of ECMWF derived cloud heights

From the ECMWF model, operationally usable cloud height information without additional costs is obtained in an 180-minute temporal resolution. The comparison is conducted for periods of 10 minutes. In Fig. 16, the scatter density plot is shown. Large deviations are present with significant bias towards lower cloud heights. The results compare well to a study comparing ECMWF derived cloud heights to ceilometer measurements, conducted on one year of data at PSA (Killius et al., 2015).

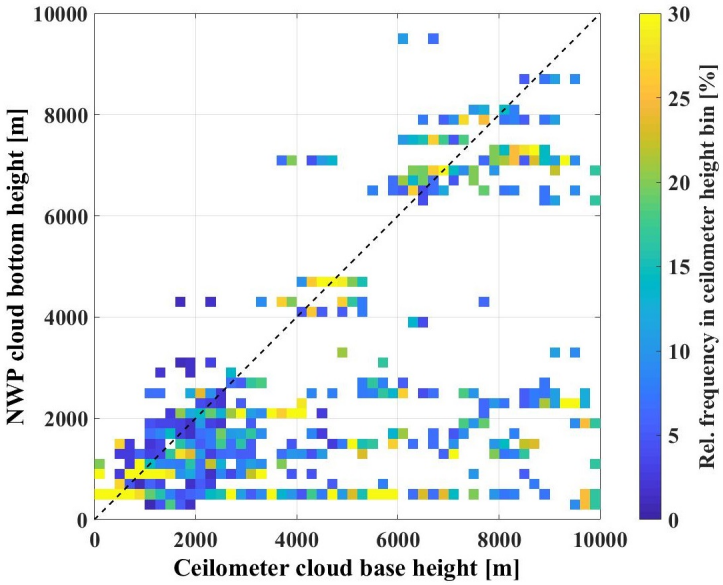

Figure 16: Scatter density plot for cloud heights on 59 days derived from NWP model ECMWF.

4.6. Cloud heights histograms

Having presented all systems in the previous sections and having looked at two example days, the histograms of the derived cloud heights from all five systems during the benchmarking campaign of 59 days are briefly discussed in this section. The 59 days are specified in Table 1 and were selected based on data availability (the CSS was installed at PSA in March 2016) and the presence of clouds.

Table 1: Periods considered for the comparisons on 59 days.

Day	Hours	Day	Hours
19/03/2016	09:00:00-17:00:00	21/08/2016	09:00:00-16:00:00
20/03/2016	10:00:00-14:00:00	25/08/2016	12:00:00-17:00:00
23/03/2016	10:00:00-14:00:00	30/08/2016	12:00:00-17:00:00
24/03/2016	12:00:00-16:00:00	31/08/2016	09:00:00-18:00:00
25/03/2016	09:00:00-13:00:00	01/09/2016	10:00:00-16:00:00
27/03/2016	13:00:00-16:00:00	02/09/2016	12:00:00-15:00:00
28/03/2016	13:00:00-17:00:00	03/09/2016	10:00:00-16:00:00
30/03/2016	10:00:00-17:00:00	04/09/2016	13:00:00-18:00:00
31/03/2016	10:00:00-15:00:00	07/09/2016	13:00:00-18:00:00
03/04/2016	11:00:00-18:00:00	13/09/2016	11:00:00-18:00:00
7/04/2016	12:00:00-16:00:00	14/09/2016	16:00:00-18:00:00
14/04/2016	12:00:00-18:00:00	15/09/2016	11:00:00-15:00:00
15/04/2016	11:00:00-17:00:00	20/09/2016	13:00:00-18:00:00
17/04/2016	12:00:00-19:00:00	23/09/2016	13:00:00-16:00:00
22/04/2016	11:00:00-19:00:00	26/09/2016	13:00:00-17:00:00
23/04/2016	11:00:00-17:00:00	27/09/2016	14:00:00-17:00:00
25/04/2016	09:00:00-14:00:00	28/09/2016	09:00:00-17:00:00
27/04/2016	10:00:00-17:00:00	29/09/2016	09:00:00-17:00:00
29/04/2016	10:00:00-18:00:00	09/10/2016	10:00:00-16:00:00
30/04/2016	10:00:00-19:00:00	14/10/2016	12:00:00-17:00:00
01/05/2016	09:00:00-17:00:00	21/10/2016	11:00:00-14:00:00
05/05/2016	12:00:00-16:00:00	28/10/2016	09:00:00-17:00:00
06/05/2016	09:00:00-18:00:00	05/11/2016	09:00:00-15:00:00
07/05/2016	11:00:00-17:00:00	10/11/2016	10:00:00-13:00:00
09/05/2016	09:00:00-19:00:00	29/11/2016	12:00:00-16:00:00
11/05/2016	11:00:00-18:00:00	01/12/2016	10:00:00-17:00:00
12/05/2016	11:00:00-18:00:00	06/12/2016	10:00:00-16:00:00
24/06/2016	15:00:00-19:00:00	07/12/2016	09:00:00-17:00:00
25/06/2016	10:00:00-18:00:00	08/12/2016	09:00:00-15:00:00
15/07/2016	09:00:00-14:00:00		

Figure 17 shows the histogram of the cloud heights derived by the ASI-CSS system (gray and solid bars) in comparison to ceilometer measurements (striped bars). As can be seen, the ASI-CSS system rarely derives cloud heights at high altitudes. The reason for this is discussed in section 4.2. The histogram of the

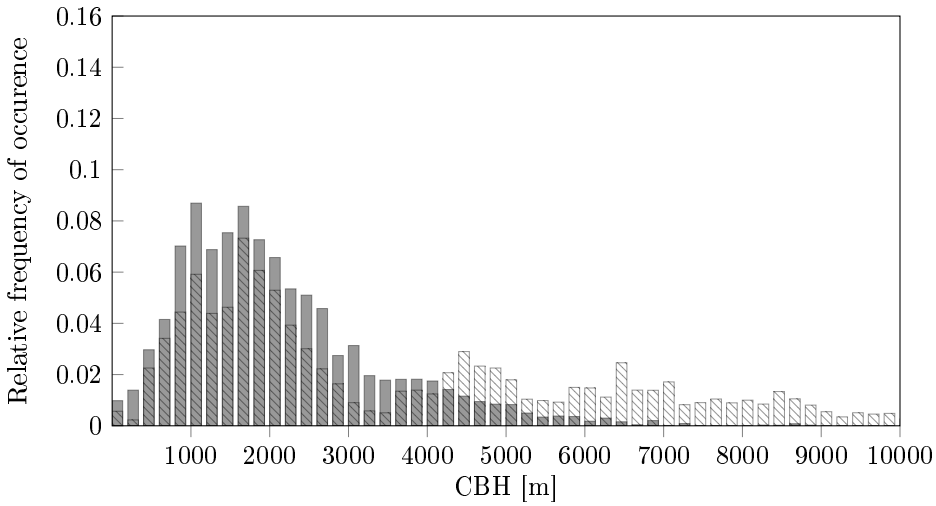

Figure 17: Histogram of the cloud heights derived from the ASI-CSS system (solid, gray) in comparison to the ceilometer measurements (white, striped) during the validation period (59 days, bin size: 200 m).

cloud heights as measured by the ASI-SC system in comparison to ceilometer measurements is shown in Fig. 18. The distribution of this system matches the distribution of the ceilometer better than the ASI-CSS system. However, for cloud heights below 1000 m, the distributions differ significantly. Figure 19 displays the histogram of the cloud heights obtained by the ASI-ASI system in comparison to the ceilometer measurements. As for the ASI-SC system, the general distribution matches with the histogram of the ceilometer measurements. In Fig. 20, the cloud height histogram from the ECMWF model are compared to ceilometer measurements, showing a certain bias towards lower cloud heights.

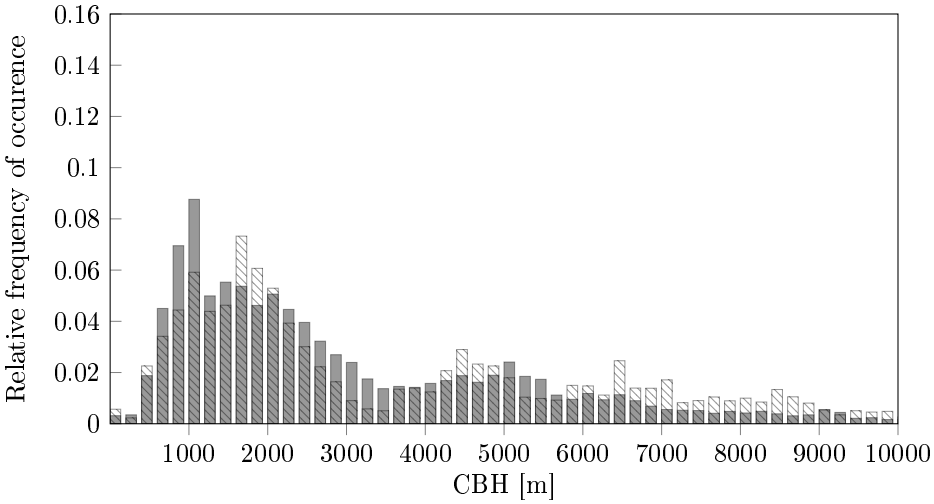

Figure 18: Histogram of the cloud heights derived from the ASI-SC system (solid, gray) in comparison to the ceilometer measurements (white, striped) during the validation period (59 days, bin size: 200 m).

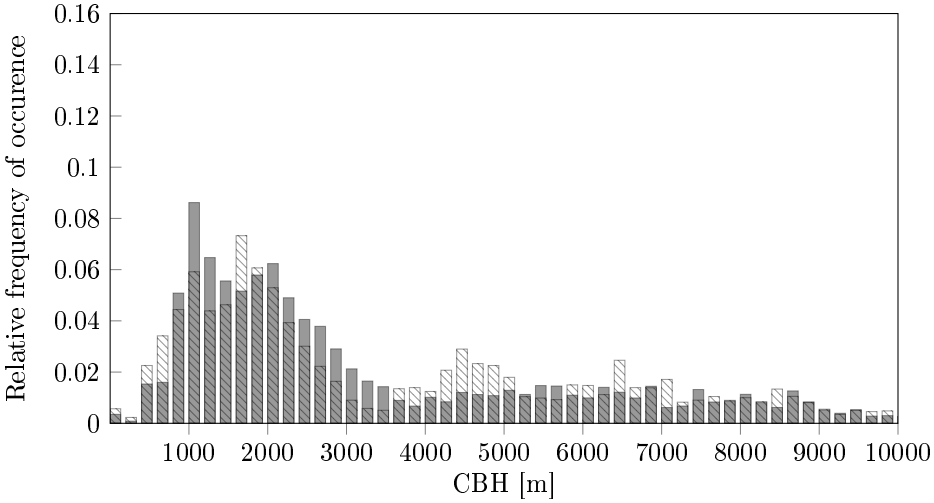

Figure 19: Histogram of the cloud heights derived from the ASI-ASI system (solid, gray) in comparison to the ceilometer measurements (white, striped) during the validation period (59 days, bin size: 200 m).

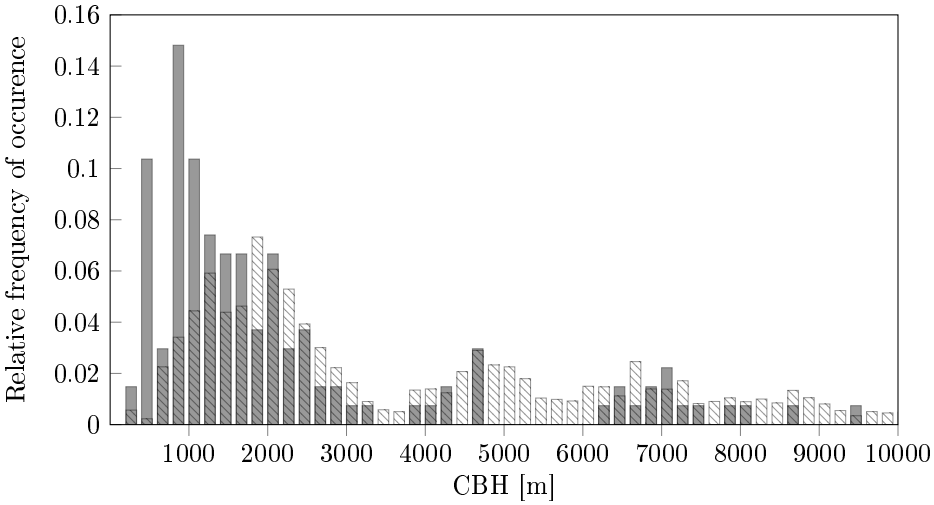

Figure 20: Histogram of the NWP cloud height data (solid, gray) in comparison to the ceilometer measurements (white, striped) during the validation period (59 days, bin size: 200 m).

4.7. Statistical deviation metrics

In Table 2, the deviations found for all three ground based systems and the NWP cloud heights on 59 days are displayed. The benchmarking is conducted for 10 minute medians for the ASI-CSS, ASI-SC and ASI-ASI system, which are compared to 10-minute median ceilometer measurements. Medians are chosen for the three benchmarked ground-based systems to eliminate the effect of outliers, which can be caused by matching errors between the binary images. For the ceilometer, the 10-minute median is used to obtain reference cloud heights.

If there is a measurement derived from a ground-based system, but the ceilometer did not measure any cloud heights within this 10 minute period, this measurement is left out. Furthermore, cloud heights above 15 km are ignored. Table 3 presents the total amount of measurements of the developed systems as well as the measurements which could be temporally matched to ceilometer measurements. ASI-ASI system provides the most measurements, 56 % more than the ASI-CSS system and 58 % more than the ASI-SC system. For the NWP cloud height data, 10 minute blocks are derived from the 180 minute temporal resolution and temporally matched with corresponding

Table 2: Benchmarking ground based systems and NWP cloud heights with ceilometer measurements: Comparison of statistical deviations found on 59 days for all cloud heights (*all*), for clouds below 5000 m and for clouds below 1000 m, as measured by the ceilometer. The validation is conducted for 10 minute temporal moving medians as described in this section.

		ASI-CSS	ASI-SC	ASI-ASI	NWP
RMSD	all	3159 m (86 %)	1614 m (44 %)	1637 m (44 %)	2770 m (75 %)
	< 5000 m	996 m (45 %)	1193 m (54 %)	826 m (38 %)	1206 m (55 %)
	< 1000 m	494 m (72 %)	690 m (100 %)	536 m (78 %)	362 m (53 %)
MAD	all	1894 m (51 %)	878 m (24 %)	872 m (24 %)	1631 m (44 %)
	< 5000 m	626 m (29 %)	593 m (27 %)	432 m (20 %)	814 m (37 %)
	< 1000 m	277 m (40 %)	321 m (47 %)	269 m (39 %)	267 m (39 %)
BIAS	all	-1528 m (-41 %)	-36 m (-1 %)	-41 m (-1 %)	1358 m (37 %)
	< 5000 m	-142 m (-6 %)	238 m (11 %)	202 m (9 %)	-533 m (-24 %)
	< 1000 m	185 m (27 %)	280 m (41 %)	247 m (36 %)	31 m (5 %)
Number of measurements	all	20082	21659	30380	1537
	< 5000 m	14713	17012	22397	1134
	< 1000 m	2039	2374	3346	192

Table 3: Total amount of measurements and measurements which can be temporally matched to ceilometer measurements of the developed systems on 59 days.

System	Total measurements	Matched measurements	%
ASI-CSS	24855	20130	81.0 %
ASI-SC	24435	21638	88.6 %
ASI-ASI	38823	30405	78.3 %

ceilometer measurements.

The deviations are specified for all cloud heights, for cloud heights below 5000 m and for cloud heights below 1000 m, as measured for the considered cloud height interval by the ceilometer. The relative deviations are calculated from the absolute deviations and the mean height as measured by the ceilometer (see Table 4).

Looking at Table 2, we see that the ASI-CSS system shows a significant RMSD, which is caused by a bias for high clouds as further discussed in section 4.2. The ASI-SC system shows similar RMSD for cloud heights below 5000 m in comparison to the ASI-CSS system, but outperforms the ASI-CSS system when all cloud heights are considered. However, if only clouds below 1000 m (as measured by the ceilometer) are included in the deviation metrics, the ASI-SC system shows the largest RMSD. Presumably, this is caused in most cases by mismatching errors during multi-layer cloud situations. The deviations of the ASI-ASI system are similar to the ASI-SC system, but it is substantially better for cloud heights below 5000 m. The NWP cloud heights show the lowest RMSD for cloud heights below 1000 m. For cloud heights below 1000 m,

Table 4: Mean cloud heights as measured by the ceilometer on 59 days.

Cloud height interval	Mean measured cloud height
all	3685 m
< 5000 m	2195 m
< 1000 m	689 m

the system with the largest bias is the ASI-SC system. As all three developed systems (ASI-CSS, ASI-SC and ASI-ASI) use the same all-sky imager derived angular information, we see that for such low cloud heights the absolute cloud velocity in [m/s] is seemingly better measured by the CSS and the ASI-ASI approach. However, although the downward-facing shadow camera (ASI-SC) and the second all-sky imager (ASI-ASI) show far larger biases for cloud heights below 1000 m in comparison to NWP and the ASI-CSS system, this apparent underperformance must be explained by the biases of the NWP and ASI-CSS system and is not a sign of higher accuracies: As these two systems tend to underestimate cloud heights, their results match the ceilometer measurements more frequently than the other systems when only clouds below 1000 m as measured by the ceilometer are considered.

The system with the overall least deviations in comparison to the ceilometer is the ASI-ASI system. The ASI-ASI system provides the most measurements, the ASI-CSS system the least. The ASI-CSS system obtains a RMSD similar to the ASI-ASI system for cloud altitudes below 1000 m, but is the least accurate if all clouds are considered. It is noteworthy that the biases of the ASI-ASI and ASI-SC system are very similar both in value and behavior. Moreover, this bias is in the order of the bias found between two ceilometers (Martucci et al., 2010) as discussed in section 2.

The statistics calculated for Table 2 are derived from a different amount of measurements (see row *Number of measurements*). This is critical: If two systems had a poor performance for e.g. clouds at high altitudes but their detection rates for such clouds were different, the system with the worse detection rate would appear to be more accurate. To consider this effect, only 10-minute time periods in which all systems provide measurements are considered for the statistics in Table 5.

Comparing the deviations found for all timestamps (Table 2) with the deviations found for the same timestamps (Table 5), we see significant changes: As the CSS rarely measures high clouds (see section 4.2), many high clouds are left out in the benchmarking for all systems in Table 5. These clouds are

Table 5: Comparing ground based systems and NWP cloud heights with the ceilometer. The results are presented as in table 2 but here only 10-minute time periods are considered in which all systems provide cloud height measurements. The validation is conducted for 10 minute temporal moving medians as described in this section.

		ASI-CSS	ASI-SC	ASI-ASI	NWP
RMSD	all	2601 m (71 %)	2596 m (70 %)	1413 m (38 %)	2475 m (67 %)
	< 5000 m	805 m (37 %)	857 m (39 %)	732 m (33 %)	1384 m (63 %)
	< 1000 m	487 m (70 %)	486 m (70 %)	499 m (72 %)	371 m (53 %)
MAD	all	1374 m (37 %)	1167 m (32 %)	683 m (19 %)	1457 m (40 %)
	< 5000 m	495 m (23 %)	473 m (22 %)	375 m (17 %)	846 m (39 %)
	< 1000 m	268 m (38 %)	273 m (39 %)	229 m (33 %)	291 m (42 %)
BIAS	all	-961 m (-26 %)	-620 m (-17 %)	-100 m (-3 %)	-934 m (-25 %)
	< 5000 m	0 m (0 %)	101 m (5 %)	156 m (7 %)	-227 m (-10 %)
	< 1000 m	201 m (29 %)	198 m (28 %)	216 m (31 %)	185 m (26 %)
Number of measurements	all	14167	14167	14167	14167
	< 5000 m	11480	11480	11480	11480
	< 1000 m	1743	1743	1743	1743

included for the other systems in Table 2. Due to that, the deviations found both for the ASI-CSS system and for the NWP cloud height data, which have biases towards low height, shrink if all heights are considered. Again, this is a statistical effect and not an indication of accuracy. Furthermore, the deviations found for the ASI-SC and ASI-ASI system, which are fairly similar in Table 2, differ notably in Table 5. This indicates that the ASI-SC system is best for high clouds, which are to some extend excluded in the calculations in Table 5 (very few CSS measurements for high clouds). The good performance of the ASI-SC system is also shown in its RMSD value for all cloud heights in Table 2, which is the lowest.

4.8. Comparison to literature

In the light of the variable cloud heights indicated e.g. in Fig. 19 and the systematic offsets, the found absolute deviations are small. As such deviations strongly depend on the weather situations and the temporal averaging applied, direct comparisons between systems tested at different areas are delicate.

If compared to the previous benchmarking of the ASI-CSS system (compared to ceilometer measurements on 27 days in San Diego, USA), relative RMSD values between 6.3 % and 29.4 % for days with average cloud heights below 1000 m are obtained by Wang et al. (2016). The much higher deviations displayed in Table 2 and 5 for cloud heights below 1000 m cannot be directly compared to these values as for the measurements clouds at higher altitudes could be present and the variability of the (multi cloud layer) situation must be considered (see image 12 and e.g. histogram 19). For one day with an average cloud height of 5864 m, an absolute RMSD of 830 m (14.2 %) is reported (Wang et al., 2016).

A system (Blanc et al., 2017), located at the PSA and based on two all-sky imagers (ASI-ASI) achieved on one example day RMSD deviations of 706 m (21.2 %), a MAD of 440 m (13.2 %) and a bias of 296 m (8.9 %). Kassianov et al. (2005) found, validated on four days and only for single-layer-cloud fields, *"that, at least for single-layer-cloud fields, moderately accurate (within 0.2 km) CBH retrieval is possible"*. A two all-sky imager based system presented in Nguyen

and Kleissl (2014) obtained smaller deviations, also on four days and also only for single homogeneous cloud layers: RMSD values between 206 m and 388 m are reported (Nguyen and Kleissl, 2014).

Once again, comparing systems benchmarked at different locations and periods is difficult as the deviations strongly depend on the weather situations during the campaign.

5. Conclusions and future work

Three low-cost, low-maintenance ground based systems are developed and compared to ceilometer reference data. Furthermore ECMWF derived cloud height data is benchmarked during the same period. As studied on 59 days, an novel approach based on two all-sky imagers is found to outperform (1) a novel system based on one all-sky imager and a downward-facing camera, (2) an adapted system based on one all-sky imager and a cloud shadow speed sensor and (3) the ECMWF cloud heights.

The system based on two all-sky imagers (ASI-ASI) showed the overall smallest deviations (19 % MAD) while obtaining the most measurements. It obtained even more measurements than the ceilometer, due to the limited field of view of the ceilometer. All-sky imagers can be deployed wherever a more or less unobstructed view on the sky is given. The all-sky imagers used here have been in active service for several years in the harsh environment of the desert of Tabernas, Spain, and were found to be very reliable. Due to the specific difference image based approach chosen, cloud detection within the images is not needed to derive cloud heights. This might hypothetically enable a less frequent cleaning routine of the cameras. The ASI-ASI system has furthermore the potential to track each cloud movement separately. This results in individual cloud heights and is currently under development. Deriving individual cloud heights is not possible with the other systems. With costs far below the cost of a ceilometer while obtaining more measurements and additionally providing two all-sky images, cloud height derivations based on this approach seems to be

a very feasible tool, especially for nowcasting systems. Future work includes a study on the optimal distance between the cameras of such a system. Also, an ASI-ASI system deriving individual cloud heights will be validated.

However, all three benchmarked ground-based systems are based on at least one all-sky imager, which cannot detect movements at night. Thus, if cloud heights during the night are needed, none of the systems are applicable in their current form. Potentially, infra-red cameras (e.g. Shaw et al. (2005), Thurairajah and Shaw (2005), Smith and Toumi (2008), Bertin et al. (2015)) could solve this issue. Potentially, larger camera exposure times at night might also work but this approach may not be feasible due to e.g. the presence of artificial light sources.

The second most promising system, consisting of a downward-facing shadow camera and an all-sky imager (ASI-SC, 32 % MAD), requires specific infrastructure or geographies such as an elevated position from a tower, lamp post or mountain and a view on an unobstructed area with little non-cloud movements and little reflecting objects. In comparison to the ASI-ASI system, the cleaning routine is further simplified as downward-facing cameras, deployed over several years in the desert of Tabernas, are found to require little cleaning. Moreover, it costs slightly less than the ASI-ASI system. The deviations found for the ASI-SC system are larger than the deviations found for the ASI-ASI system.

For clouds below 5000 m, the ASI-CSS system, including one all-sky imager and a cloud shadow speed sensor, shows similar deviations in comparison to the ASI-ASI system. Considering the costs of the deployed equipment, this system might be the cheapest (although the CSS is currently not commercially available). However, optically thin clouds and clouds with diffuse edges pose a challenge for the ASI-CSS system (37 % MAD). If such clouds are not present or not of interest, this system is a practical tool to derive cloud motion vectors. The CSS has a very user friendly cleaning and maintenance routine: After more than one year in the desert of Tabernas, the CSS was never cleaned and is still found to be operational without accuracy restrictions.

The cloud height data from the ECMWF NWP model show similar devia-

tions like the ASI-CSS system and are significantly less accurate (40 % MAD) in comparison to the ASI-ASI system. Using NWP derived cloud base heights might thus not be an option for all-sky imager based solar nowcasting systems. Potentially, improving the modeling of cirrus clouds which are often not represented in the global ECMWF model and higher resolved local area models could change this.

All presented systems can provide crucial cloud height information for solar nowcasting systems, which help to cope with the inherent variability of the solar resource. If this variability can be managed, solar grid penetrations far above the current levels can be reached. Other applications for such low-cost systems may be found in the fields of meteorology as well as commercial and private aviation.

Acknowledgements

The research presented in this paper has received funding from the European Union's Horizon 2020 programme for the initial development of the shadow camera system (PreFlexMS, Grant Agreement no. 654984). With funding from the German Federal Ministry for Economic Affairs and Energy within the WobaS project, all-sky imager systems and the shadow camera system were further developed. The European Union's FP7 programme under Grant Agreement no. 608623 (DNICast project) financed operations of the all-sky imagers and other ground measurements. We furthermore thank the University of San Diego for providing us with the CSS. The authors are also grateful for the financial support provided by project PRESOL with reference ENE2014-59454-C3-2-R, funded by the Ministerio de Economía y Competitividad and co-financed by the European Regional Development Fund (FEDER). Thanks to the colleagues from the Solar Concentrating Systems Unit of CIEMAT for the support provided in the installation and maintenance of the shadow cameras. These instruments are installed on CIEMAT's CESA-I tower of the Plataforma Solar de Almería.

References

Allmen, M. C., Kegelmeyer Jr, W. P., 1996. The Computation of Cloud-Base Height from Paired Whole-Sky Imaging Cameras. Journal of Atmospheric and Oceanic Technology 13 (1), 97–113.
URL http://journals.ametsoc.org/doi/abs/10.1175/1520-0426(1996)013%3C0097:TCOCBH%3E2.0.CO%3B2

Beekmans, C., Schneider, J., Läbe, T., Lennefer, M., Stachniss, C., Simmer, C., 2016. Cloud photogrammetry with dense stereo for fisheye cameras. Atmospheric Chemistry and Physics 16 (22), 14231–14248.
URL http://dx.doi.org/10.5194/acp-16-14231-2016

Bernecker, D., Riess, C., Christlein, V., Angelopoulou, E., Hornegger, J., 2013. Representation Learning for Cloud Classification. Springer Berlin Heidelberg, Berlin, Heidelberg, pp. 395–404.
URL http://dx.doi.org/10.1007/978-3-642-40602-7_42

Bertin, C., Cros, S., Saint-Antonin, L., Schmutz, N., 2015. Prediction of optical communication link availability: real-time observation of cloud patterns using a ground-based thermal infrared camera. Proc. SPIE 9641, 96410A–96410A–8.
URL http://dx.doi.org/10.1117/12.2194920

Blanc, P., Massip, P., Kazantzidis, A., Tzoumanikas, P., Kuhn, P., Wilbert, S., Schüler, D., Prahl, C., 2017. Short-Term Forecasting of High Resolution Local DNI Maps with Multiple Fish-Eye Cameras in Stereoscopic Mode. AIP Conference Proceedings 1850 (1), 140004.
URL http://aip.scitation.org/doi/abs/10.1063/1.4984512

Chen, X., Du, Y., Wen, H., June 2017. Forecasting based power ramp-rate control for PV systems without energy storage. In: 2017 IEEE 3rd International Future Energy Electronics Conference and ECCE Asia (IFEEC 2017 - ECCE Asia). pp. 733–738.
URL http://ieeexplore.ieee.org/abstract/document/7992130/

Cros, S., Liandrat, O., Sébastien, N., Schmutz, N., July 2014. Extracting cloud motion vectors from satellite images for solar power forecasting. In: 2014 IEEE Geoscience and Remote Sensing Symposium. pp. 4123–4126.
URL http://ieeexplore.ieee.org/document/6947394/

Fernandez-Jimenez, L. A., noz Jimenez, A. M., Falces, A., Mendoza-Villena, M., Garcia-Garrido, E., Lara-Santillan, P. M., Zorzano-Alba, E., Zorzano-Santamaria, P. J., 2012. Short-term power forecasting system for photovoltaic plants. Renewable Energy 44, 311 – 317.
URL http://www.sciencedirect.com/science/article/pii/S0960148112001516

Fung, V., Bosch, J. L., Roberts, S. W., Kleissl, J., 2013. Cloud shadow speed sensor. Atmospheric Measurement Techniques 6 (5).
URL http://dx.doi.org/10.5194/amt-7-1693-2014

Hammer, A., Heinemann, D., Lorenz, E., LÃijckehe, B., 1999. Short-term forecasting of solar radiation: a statistical approach using satellite data. Solar Energy 67 (1), 139 – 150.
URL http://www.sciencedirect.com/science/article/pii/S0038092X00000384

Huang, H., Yoo, S., Yu, D., Huang, D., Qin, H., 2012. Correlation and local feature based cloud motion estimation. In: Proceedings of the Twelfth International Workshop on Multimedia Data Mining. MDMKDD '12. ACM, New York, NY, USA, pp. 1–9.
URL http://doi.acm.org/10.1145/2343862.2343863

Kassianov, E., Long, C. N., Christy, J., 2005. Cloud-Base-Height Estimation from Paired Ground-Based Hemispherical Observations. Journal of Applied Meteorology 44 (8), 1221–1233.
URL http://dx.doi.org/10.1175/JAM2277.1

Kazantzidis, A., Tzoumanikas, P., Bais, A., Fotopoulos, S., Economou, G.,

2012. Cloud detection and classification with the use of whole-sky ground-based images. Atmospheric Research 113, 80 – 88.
URL http://www.sciencedirect.com/science/article/pii/S0169809512001342

Kazantzidis, A., Tzoumanikas, P., Blanc, P., Massip, P., Wilbert, S., Ramirez-Santigosa, L., 2017. 5 - short-term forecasting based on all-sky cameras. In: Kariniotakis, G. (Ed.), Renewable Energy Forecasting. Woodhead Publishing Series in Energy. Woodhead Publishing, pp. 153 – 178.
URL http://www.sciencedirect.com/science/article/pii/B9780081005040000056

Killius, N., Prahl, C., Hanrieder, N., Wilbert, S., Schroedter-Homscheidt, M., 09 2015. On the use of NWP for Cloud Base Height Estimation in Cloud Camera-Based Solar Irradiance Nowcasting. Oral presenation on EUPVSEC.
URL http://www.eupvsec-planner.com/presentations/c32772/on_the_use_of_nwp_for_cloud_base_height_estimation_in_cloud_camera-based_solar_irradiance_nowcasting.htm

Kuhn, P., Nouri, B., Wilbert, S., Prahl, C., Kozonek, N., Schmidt, T., Yasser, Z., Ramirez, L., Zarzalejo, L., Meyer, A., Vuilleumier, L., Heinemann, D., Blanc, P., Pitz-Paal, R., 2017a. Validation of an all-sky imager-based nowcasting system for industrial PV plants. Progress in Photovoltaics: Research and Applications.
URL http://dx.doi.org/10.1002/pip.2968

Kuhn, P., Wilbert, S., Prahl, C., Garsche, D., Schüler, D., Haase, T., Ramirez, L., Zarzalejo, L., Meyer, A., Blanc, P., Pitz-Paal, R., 2018. Applications of a shadow camera system for energy meteorology. Advances in Science and Research 15, 11–14.
URL https://www.adv-sci-res.net/15/11/2018/

Kuhn, P., Wilbert, S., Prahl, C., Schüler, D., Haase, T., Hirsch, T., Wittmann, M., Ramirez, L., Zerzalejo, L., Meyer, A., Vuilleumier, L., Blanc, P.,

Pitz-Paal, R., 2017b. Shadow camera system for the generation of solar irradiance maps. Solar Energy 157, 157 – 170.
URL http://www.sciencedirect.com/science/article/pii/S0038092X17304814

Kuhn, P., Wirtz, M., Wilbert, S., Bosch, J., Heinemann, D., Kleissl, J., Pitz-Paal, R., 2017c. Field validation and bechmarking of a cloud shadow speed sensor. submitted to Solar Energy.

Lave, M., Kleissl, J., Ellis, A., Mejia, F., June 2013. Simulated PV power plant variability: Impact of utility-imposed ramp limitations in Puerto Rico. In: 2013 IEEE 39th Photovoltaic Specialists Conference (PVSC). pp. 1817–1821.
URL http://ieeexplore.ieee.org/abstract/document/6744495/

Marcos, J., Storkël, O., Marroyo, L., Garcia, M., Lorenzo, E., 2014. Storage requirements for PV power ramp-rate control. Solar Energy 99, 28 – 35.
URL http://www.sciencedirect.com/science/article/pii/S0038092X13004672

Martucci, G., Milroy, C., O'Dowd, C. D., 2010. Detection of Cloud-Base Height Using Jenoptik CHM15K and Vaisala CL31 Ceilometers. Journal of Atmospheric and Oceanic Technology 27 (2), 305–318.
URL http://dx.doi.org/10.1175/2009JTECHA1326.1

Nguyen, A., Velay, M., Schoene, J., Zheglov, V., Kurtz, B., Murray, K., Torre, B., Kleissl, J., 2016. High PV penetration impacts on five local distribution networks using high resolution solar resource assessment with sky imager and quasi-steady state distribution system simulations. Solar Energy 132, 221 – 235.
URL http://www.sciencedirect.com/science/article/pii/S0038092X16002061

Nguyen, D. A., Kleissl, J., 2014. Stereographic methods for cloud base height determination using two sky imagers. Solar Energy 107, 495–509.
URL http://dx.doi.org/10.1016/j.solener.2014.05.005

Perez, R., David, M., Hoff, T. E., Jamaly, M., Kivalov, S., Kleissl, J., Lauret, P., Perez, M., 2016. Spatial and temporal variability of solar energy. Foundations and Trends in Renewable Energy 1 (1), 1–44.
URL http://dx.doi.org/10.1561/2700000006

Scaramuzza, D., Martinelli, A., Siegwart, R., 2006. A toolbox for easily calibrating omnidirectional cameras. In: 2006 IEEE/RSJ International Conference on Intelligent Robots and Systems. IEEE, pp. 5695–5701.
URL http://ieeexplore.ieee.org/abstract/document/4059340/

Seiz, G., Shields, J., Feister, U., Baltsavias, E., Gruen, A., 2007. Cloud mapping with ground-based photogrammetric cameras. International Journal of Remote Sensing 28 (9), 2001–2032.
URL http://dx.doi.org/10.1080/01431160600641822

Shaw, J. A., Nugent, P. W., Pust, N. J., Thurairajah, B., Mizutani, K., Jul 2005. Radiometric cloud imaging with an uncooled microbolometer thermal infrared camera. Opt. Express 13 (15), 5807–5817.
URL http://www.opticsexpress.org/abstract.cfm?URI=oe-13-15-5807

Shuigen, W., Zhen, C., Hua, D., May 2009. Motion Detection Based on Temporal Difference Method and Optical Flow field. In: 2009 Second International Symposium on Electronic Commerce and Security. Vol. 2. pp. 85–88.
URL http://ieeexplore.ieee.org/document/5209870/

Singla, N., 2014. Motion detection based on frame difference method. International Journal of Information & Computation Technology 4 (15), 1559–1565.
URL https://www.ripublication.com/irph/ijict_spl/ijictv4n15spl_10.pdf

Smith, S., Toumi, R., 2008. Measuring Cloud Cover and Brightness Temperature with a Ground-Based Thermal Infrared Camera. Journal of Applied Meteorology and Climatology 47 (2), 683–693.
URL http://dx.doi.org/10.1175/2007JAMC1615.1

Thurairajah, B., Shaw, J. A., Sept 2005. Cloud statistics measured with the infrared cloud imager (ici). IEEE Transactions on Geoscience and Remote Sensing 43 (9), 2000–2007.
URL http://ieeexplore.ieee.org/document/1499016/

Urquhart, B., Ghonima, M., Nguyen, D. A., Kurtz, B., Chow, C. W., Kleissl, J., 2013. Chapter 9 - Sky-Imaging Systems for Short-Term Forecasting. In: Kleissl, J. (Ed.), Solar Energy Forecasting and Resource Assessment. Academic Press, Boston, pp. 195 – 232.
URL http://www.sciencedirect.com/science/article/pii/B9780123971777000097

Wang, G., Kurtz, B., Kleissl, J., 2016. Cloud base height from sky imager and cloud speed sensor. Solar Energy 131, 208–221.
URL http://dx.doi.org/10.1016/j.solener.2016.02.027

Wang, J., Rossow, W. B., 1995. Determination of Cloud Vertical Structure from Upper-Air Observations. Journal of Applied Meteorology 34 (10), 2243–2258.
URL http://journals.ametsoc.org/doi/abs/10.1175/1520-0450(1995)034%3C2243%3ADOCVSF%3E2.0.CO%3B2

Wilbert, S., Nouri, B., Prahl, C., Garcia, G., Ramirez, L., Zarzalejo, L., Valenzuela, L., Ferrera, F., Kozonek, N., Liria, J., 2016. Application of Whole Sky Imagers for Data Selection for Radiometer Calibration. EU PVSEC 2016 Proceedings, 1493–1498.
URL http://dx.doi.org/10.4229/EUPVSEC20162016-5A0.8.6

Yang, D., Kleissl, J., Gueymard, C. A., Pedro, H. T., Coimbra, C. F., 2018. History and trends in solar irradiance and {PV} power forecasting: A preliminary assessment and review using text mining. Solar Energy, –.
URL https://www.sciencedirect.com/science/article/pii/S0038092X17310022

Yang, H., Kurtz, B., Nguyen, D., Urquhart, B., Chow, C., Ghonima, M., Kleissl, J., 2014. Solar irradiance forecasting using a ground-based sky imager

developed at UC San Diego. Solar Energy 103, 502–524, cited By 48.

URL http://www.sciencedirect.com/science/article/pii/S0038092X14001327